Distances to Recent Near-Earth Supernovae from Geological and Lunar ^{60}Fe

Adrienne F. Ertel[1,2] and Brian D. Fields[1,2,3]

[1] Department of Astronomy, University of Illinois, Urbana, IL 61801, USA
[2] Illinois Center for the Advanced Study of the Universe, University of Illinois, Urbana, IL 61801, USA
[3] Department of Physics, University of Illinois, Urbana, IL 61801, USA

Abstract

Near-Earth supernova blasts which engulf the solar system have left traces of their ejecta in the geological and lunar records. There is now a wealth of data on live radioactive ^{60}Fe pointing to a supernova at 3 Myr ago, as well as the recent discovery of an event at 7 Myr ago. We use the available measurements to evaluate the distances to these events. For the better analyzed supernova at 3 Myr, samples include deep-sea sediments, ferromanganese crusts, and lunar regolith; we explore the consistency among and across these measurements, which depends sensitively on the uptake of iron in the samples as well as possible anisotropies in the ^{60}Fe fallout. There is also significant uncertainty in the astronomical parameters needed for these calculations. We take the opportunity to perform a parameter study on the effects that the ejected ^{60}Fe mass from a core-collapse supernova and the fraction of dust that survives the remnant have on the resulting distance. We find that with an ejected ^{60}Fe mass of $3 \times 10^{-5} \, M_\odot$ and a dust fraction of 10%, the distance range for the supernova 3 Myr ago is $D \sim 20$–140 pc, with the most likely range between 50 and 65 pc. Using the same astrophysical parameters, the distance for the supernova at 7 Myr ago is $D \sim 110$ pc. We close with a brief discussion of geological and astronomical measurements that can improve these results.

Unified Astronomy Thesaurus concepts: Supernovae (1668); Nucleosynthesis (1131); Nuclear abundances (1128); Mass spectrometry (2094); Astrophysical dust processes (99)

1. Introduction

In the last few decades, two global ^{60}Fe ($t_{1/2} = 2.62$ Myr[4]) signals corresponding to near-Earth supernovae have been discovered in ferromanganese (FeMn) crusts and deep-sea sediments at 3 and 7 million years ago (Mya; Knie et al. 1999, 2004; Fitoussi et al. 2008; Ludwig et al. 2016; Wallner et al. 2016, 2021). An excess of ^{60}Fe above the natural background has also been discovered in lunar regolith (Fimiani et al. 2016). The progenitors of these signals are most likely either core-collapse supernovae (CCSNe) or electron-capture supernovae (ECSNe), as other producers of ^{60}Fe, such as thermonuclear supernovae and kilonovae, do not produce sufficient ^{60}Fe mass to be within a plausible distance of Earth (Fry et al. 2015). Although not entirely ruled out, super-asymptotic-giant-branch (AGB) stars are not considered in this paper, as their slow winds last a relatively short duration and do not match the observed ^{60}Fe fallout timescale of $\gtrsim$1 Myr (Ertel et al. 2023). The two near-Earth supernovae conveniently fall into separate geologic epochs, and therefore we will refer to them as the Pliocene Supernova (SN Plio, 3 Mya) and the Miocene Supernova (SN Mio, 7 Mya). For recent reviews on near-Earth supernovae, see Fields & Wallner (2023), Korschinek & Faestermann (2023), and Wallner (2023).

Fry et al. (2015) used the available data from Knie et al. (2004) and Fitoussi et al. (2008) to put bounds on the distance from Earth to SN Plio given the observed ^{60}Fe fluence. Using

the supernova ^{60}Fe yields available at the time, they found a distance of $D \sim 60$–130 pc for CCSNe and ECSNe. We seek to expand on those calculations, given the plethora of new ^{60}Fe data for SN Plio presented in Fimiani et al. (2016), Ludwig et al. (2016), Wallner et al. (2016), and Wallner et al. (2021). In addition to the Earth-based data, the distances to the supernova depend on three astronomical parameters: the ejected ^{60}Fe mass from the progenitor, the time it takes for the dust to travel to Earth, and the fraction of the dust which survives the journey. The time is thus ripe to investigate the impact those parameters have on the supernova distance.

The structure for the paper is as follows. In Section 2, we lay out the relevant variables and their theory and data sources. In Section 3, we examine the different ^{60}Fe samples and their possible constraints. In Section 4, we examine the three main astronomical parameters, their bounds, and the implications of their ranges on the supernova distance. We then systematically map out the uncertainties in those parameters in Section 5 and rule out model combinations. In Section 6, we discuss other methods for calculating the supernova distance.

2. Formalism

The nucleosynthesis products from a supernova—including radioisotopes such as ^{60}Fe—are ejected in the explosion and eventually spread throughout the remnant. The time-integrated flux, or fluence, thus allows us to connect the observed parameters of the ^{60}Fe signal on Earth with the astronomical parameters of the supernova remnant (SNR). In reality, the distribution of ^{60}Fe in the remnant will be anisotropic, and the time history of its flux on Earth will be complex. Because the supernova blast cannot compress the solar wind to 1 au without being within 10 pc where event rates are low (Fields et al. 2008; Miller & Fields 2022), the terrestrial signal can arise only from the ejecta arriving in the form of dust grains

---

[4] Half-life measurement: Rugel et al. (2009), Wallner et al. (2015), and Ostdiek et al. (2017).

(Benítez et al. 2002; Athanassiadou & Fields 2011; Fry et al. 2015, 2016). We have argued that supernova dust decouples from the blast plasma, and that its magnetically dominated propagation and evolution naturally lead to the observed >1 Myr timescale for ^{60}Fe deposition by spreading the dust throughout the remnant (Fry et al. 2020; Ertel et al. 2023). The Earth's motion relative to the blast will also affect the ^{60}Fe flux onto Earth (Chaikin et al. 2022).

The ^{60}Fe flux $\Phi_{60}(t)$ accumulates in natural archives over time. This signal integrates to give the ^{60}Fe fluence $\mathcal{F} = \int \Phi_{60}(t) \, dt$, which will be the central observable in our analysis. Our goal in this paper, as with earlier distance studies (Fields & Ellis 1999; Fry et al. 2015), is not to capture all of this complexity, but to find a characteristic distance based on a simplified picture of a spherical blast engulfing a stationary Earth.

For a spherical supernova blast, we can generalize the relationship between the observed fluence of a radioisotope i and the supernova properties as

$$\mathcal{F}_{\text{obs},i} = \frac{1}{4} \frac{M_{\text{ej},i}}{4\pi D^2 A_i m_u} U_i f_i \exp\left[\frac{-(t_{\text{arrive}} + t_{\text{trav}})}{\tau_i}\right], \quad (1)$$

where A_i is the mass number, m_u is the atomic mass unit, and τ_i is the lifetime of the isotope. The leading factor of $1/4$ is the ratio of Earth's cross-sectional area to surface area. The two Earth-based parameters are the arrival time t_{arrive}, which is the time of the first nonzero signal point, and the uptake fraction U_i, which quantifies the difference between the amount of the isotope that arrives at Earth and what is detected (see Section 3). The four astronomical parameters are the ejected mass of the isotope $M_{\text{ej},i}$, the fraction of the isotope that is in the form of dust f_i, the distance to the supernova D, and the travel time t_{trav} between the supernova and Earth. Note that Equation (1) assumes a uniform fallout of the ^{60}Fe onto Earth (but see Fry et al. 2016).

Equation (1) gives an inverse square law for the radioisotope fluence as a function of distance, similar to the inverse square relation for photon flux. Setting aside the travel time's dependence on the distance, we can then solve Equation (1) as

$$D = \frac{1}{2}\left(\frac{f_{60} M_{\text{ej},60}}{4\pi A_{60} m_u}\right)^{\frac{1}{2}} \left(\frac{U_{60}}{\mathcal{F}_{\text{obs}}}\right)^{\frac{1}{2}} \times \exp\left[\frac{-(t_{\text{arrive}} + t_{\text{trav}})}{2\,\tau_{60}}\right]. \quad (2)$$

Equation (2) is the main equation of interest in this work; therefore we have substituted the generic isotope i for ^{60}Fe, as this is the isotope measured on Earth. In the interest of brevity, $\mathcal{F}_{\text{obs},60}$ will be referred to as $\mathcal{F}_{\text{obs}}$. Note that $\mathcal{F}_{\text{obs}}$ is the fluence of ^{60}Fe into the material (deep-sea sediment, FeMn crust, or lunar regolith) and not the ^{60}Fe fluence at Earth's orbit or in the interstellar medium (ISM)—these latter two are a geometric factor of 4 different due to surface area and include corrective values such as the uptake factor.

Equation (2) shows that distance scales as $D \propto (f_{60} \, \mathcal{N}_{60}/\mathcal{F}_{\text{obs}})^{1/2}$. We see the fluence scaling $\mathcal{F}_{\text{obs}}^{-1/2}$ and additional dimensionless factors counting the number $\mathcal{N}_{60} = M_{\text{ej},60}/A_{60} m_u$ of ^{60}Fe atoms and correcting for the dust fraction f_{60}. Moreover, the analogy to photon flux is very close: this *radioactivity distance* is formally

identical to a luminosity distance, with (uptake corrected) ^{60}Fe fluence playing the role of photon flux, and the product $f_{60} \times M_{\text{ej},60}$ of dust fraction and yield playing the role of luminosity.

The error on the radioactivity distance depends on both data-driven and astrophysical values. Because an objective of this work is to examine the effects that different ejected masses, dust fractions, and travel times have on the supernova distance, the errors associated with those values are not included in our calculations. Therefore the quoted distance error will only be the result of the data-driven values of observed fluence and uptake factor.[5]

All observed fluences have well-defined statistical errors. However most of the uptake factors are quoted as an approximation or assumed to be 100%—due to the lack of clarity and the large influence these errors have on the resulting distance, for the purpose of this paper we will not be including the uptake error explicitly into our calculations. Rather, we will illustrate the effect of this systematic error by displaying results for a wide range of uptakes corresponding to values quoted in the literature. The errors quoted on all of our distance calculations therefore solely reflect the reported statistical error on the fluence.

We can calculate the error on the radioactivity distance that arises due to uncertainties in the fluence. This is simply

$$\sigma_D = \frac{1}{2} D \left(\frac{\sigma_{\mathcal{F}}}{\mathcal{F}_{\text{obs}}}\right), \quad (3)$$

where $\sigma_{\mathcal{F}}$ is the error on the observed fluence.

It is important to note that the radioactivity distance scales as $D \propto \sqrt{f_{60} \, M_{\text{ej},60}}$, so that the key astrophysical input or figure of merit is the product $f_{60} \times M_{\text{ej},60}$ of ^{60}Fe yield and dust fraction. This represents physically the effective yield of ^{60}Fe in a form able to reach the Earth. The resulting radioactivity distance is therefore most affected by the allowed range of $M_{\text{ej},60}$ and f_{60}. To that effect, this paper presents the quantity $f_{60} \times M_{\text{ej},60} \, [M_\odot]$ as a means of approximating the maximum and minimum astronomical parameters that can be used to find a supernova's distance from Earth.

3. Data and Benchmark Results

The data used in this analysis are from the work of Knie et al. (2004, hereafter K04), Fitoussi et al. (2008, hereafter F08), Ludwig et al. (2016, hereafter L16), Wallner et al. (2016, hereafter W16), Fimiani et al. (2016, hereafter F16), and Wallner et al. (2021, hereafter W21). The ^{60}Fe signal has been found in a number of different materials on Earth, including deep-sea sediment cores and FeMn crusts, as well as in the lunar regolith.

FeMn crusts are slow-growing, iron and manganese-rich layers which build up on exposed rock surfaces in the ocean at a rate of a few millimeters per megayear. Ferromanganese nodules have a similar growth rate and are found as individual objects on the sea floor. These crusts grow by extracting iron and manganese from the surrounding seawater, and thus they have an associated uptake factor, which accounts for how much of the available iron in the seawater they absorb. The uptake factor varies considerably with each crust, on the order of 1%–

---

[5] The arrival time also has an associated error, which contributes a distance error in $\sigma(D)/D = \sigma(t_{\text{arr}}/2\tau)$, which is always much less than the other contributions to the uncertainty.

Table 1
Data-driven Values for Calculating the Distance to SN Plio

Paper		$\mathcal{F}_{obs}$ (10^6 atoms cm^{-2})	t_{arr} (Myr)	U_{60}	D (pc)
Knie et al. (2004) crust[a]	K04	1.5 ± 0.4	2.61	~ 0.006	22 ± 3
Knie et al. (2004) crust		1.5 ± 0.4	2.61	~ 0.24[b]	140 ± 19
Knie et al. (2004) crust		1.5 ± 0.4	2.61	~ 0.04[c]	57 ± 8
Fitoussi et al. (2008) sediment A	F08	30.0 ± 14.5[d]	2.87	1.0	64 ± 15
Fitoussi et al. (2008) sediment B		58.0 ± 39.0[d]	3.08	1.0	46 ± 15
Ludwig et al. (2016) sediment	L16	0.56 ± 0.18	3.02[e]	1.0	470 ± 75
Wallner et al. (2016) sediment	W16	35.4 ± 2.6	3.18	1.0	58.9 ± 2.2
Wallner et al. (2016) crust 1		5.9 ± 0.8	4.35	0.17 ± 0.3	59 ± 4
Wallner et al. (2016) crust 2		2.2 ± 0.2	3.1	~ 0.07	62 ± 3
Wallner et al. (2016) nodules		1.4 ± 0.5	3.3	0.02–0.04	51 ± 9
Wallner et al. (2021) crust 3	W21	6.10 ± 0.31	4.2	0.17 ± 0.3	58.3 ± 1.5
Fimiani et al. (2016) lunar	F16	10–60	2.6	1.0	45–110

Notes. $\mathcal{F}_{obs}$ is the fluence into the material (sediment, FeMn crust, FeMn nodule, or lunar regolith); t_{arr} is the arrival time of the dust on Earth, when the ^{60}Fe signal starts; and U_{60} is the uptake percentage of ^{60}Fe into the material, with sediments and lunar regolith assumed to have a 100% uptake. The example of a possible distance D to SN Plio quoted here is calculated assuming $M_{ej,60} \times f_{60} = 3 \times 10^{-6}\ M_\odot$, with $M_{ej,60} = 3 \times 10^{-5}\ M_\odot$ and $f_{60} = 0.1$.
[a] $\mathcal{F}_{obs}$ and t_{arr} are from W16 Table 3 (corrected for ^{60}Fe and ^{10}Be half-life changes since the publication of K04); uptake is the original quoted in K04 (see Section 3.1).
[b] Uptake is from the discussion in F16 (see Section 3.1).
[c] Uptake is calculated from the W16 sediment (see Section 3.1).
[d] Fluence values are not specifically quoted in the original paper; these have been calculated using the area under the curve for Figures 4(A) and (B) in F08 (see Section 3.2).
[e] L16 states that the signal starts at 2.7 ± 0.1 Mya, however the first nonzero binned point in their Figure 2(B) is 3.02 Myr; we use the 3.02 Myr start point here.

30% (see Table 1), and must be calculated for each sample. In contrast, deep-sea sediments grow much faster rate of a few millimeters per kiloyear. Unlike FeMn crusts, they are assumed to have a 100% uptake factor as they sample what is deposited on the ocean floor.

Table 1 summarizes the observed fluences ($\mathcal{F}_{obs}$), the ^{60}Fe arrival times (on Earth and the Moon), and the uptake percentage of ^{60}Fe into the material for all of the ^{60}Fe detections considered in this work.[6] We see that the arrival times are for the most part quite consistent, even across the crust and sediment measurements.

Table 1 also provides an example of a distance to SN Plio. These results all use the quoted fluence and uptake, and assume $f_{60} \times M_{ej,60} = 3 \times 10^{-6}\ M_\odot$. In the next sections, we will address in detail the correlations between these results and the wide variety of distances they give. The range of distances is much larger than the quoted statistical errors, confirming that systematic errors—most notably the uptake—dominate the distance uncertainties.

Figure 1 then plots the distance versus fluence for the published ^{60}Fe data relating to SN Plio. The distance is calculated as shown in Table 1 and the fluence refers to the fluence into the material on Earth. The error bars on the fluence are as quoted in the original papers; the error bars on the distance trace the fluence error effects.[7] The top plot of Figure 1

shows all of the data, while the bottom plot neglects the outlier L16 sediment data (discussed in Section 3.3).

Figure 1 represents a consistency check among the ^{60}Fe measurements. The reported fluence and uptake are used to infer the interstellar fluence arriving at Earth, and this in turn leads to the distances plotted. As seen in Equation (2), all results scale with the adopted yield and dust faction as $D \propto (f_{60}M_{ej,60})^{1/2}$. Because this factor is common to all points shown in the plot, the entire pattern can shift up or down systematically for different choices of this parameter combination. But crucially, whether the distances we infer are consistent or discrepant do not depend on these parameter choices.

We will review the agreement among data sets in detail below, but the main results are clear from a glance at Figure 1. We see that most results span 50–150 pc, which are shown in a zoom-in view of the bottom panel. There is a group of data clustered together in distance, from around 40 to 70 pc, which shows a nontrivial consistency—though we will see that most of the points are correlated. Note that the K04 crust results are shown for different uptake values, making it clear that this choice can lead to consistency (if $U_{60} \sim 0.04$ for this crust) or discrepancy (if U_{60} takes a substantially different value). On the other hand, the top panel shows that the L16 results lead to distances that are far from the others. We discuss this in detail below.

The horizontal lines on Figure 1 indicate key astrophysical distances. The lowest line at 10 pc is an estimate of the typical SN lethal distance, inside of which substantial damage to the biosphere is expected (e.g., Gehrels et al. 2003; Brunton et al. 2023). No points lie below this range, consistent with the lack of widespread anomalous biological extinctions in the past 3 Myr. The other two lines show the position of nearby star

---

[6] A low-level ^{60}Fe infall over the last 30 kyr has been measured by Koll et al. (2019) and Wallner et al. (2020); however, we do not consider it as part of the same astrophysical delivery mechanism that created the ^{60}Fe peaks considered in this work and therefore this infall is not included.
[7] As can be seen in Table 1, only the W16 crust 1 and W21 crust 3 values have precise errors on the uptake (the sediment and lunar uptakes are assumed to be 100% and thus do not have an associated error). Without more precise values for the other FeMn crust uptakes and in the interest of consistency between data sets, we ignore all uptake errors here.
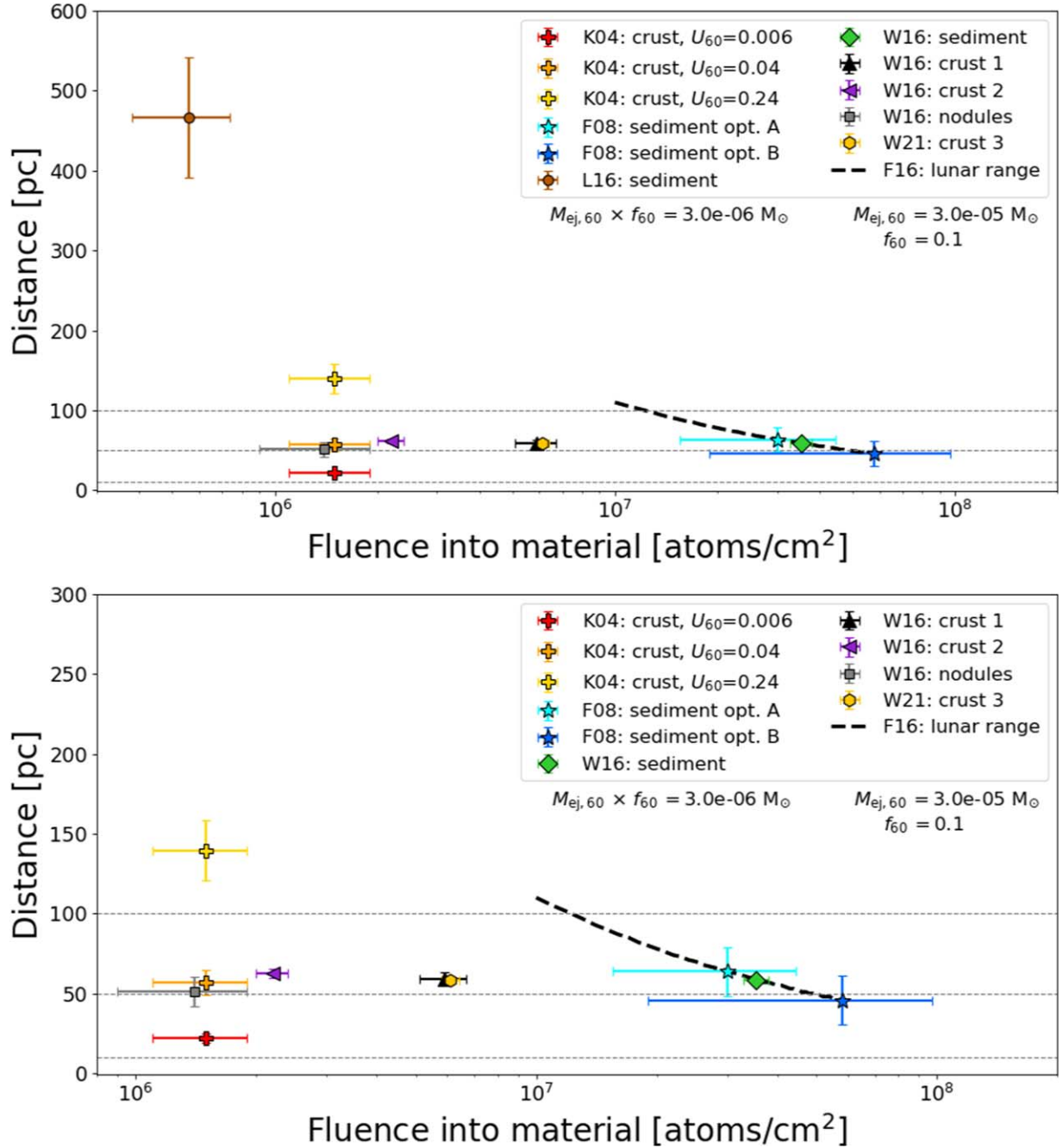
Figure 1. Distance to supernova vs. fluence into material for SN Plio (3 Mya). The assumed $f_{60} \times M_{ej,60}$ is printed under the legend. The horizontal dotted lines show distances of 100, 50, as well as 10 pc (the lethal distance). Top: all of the ^{60}Fe fluence data, including L16. K04 is shown with three possible uptake factors (see Section 3.1), demonstrating the effect of the uptake on the distance. F08 sediment opt. A and B are two different binnings for the same sediment data, not two sediments (see Section 3.2). Note that all of the W16 and W21 data, as well as that of K04 ($U_{60} = 0.4$, orange cross), are correlated to the W16 sediment data and therefore show approximately the same distance to SN. Bottom: a zoom-in look of the distances without the L16 point. For paper citations, abbreviations, as well as calculation details, see Table 1.

clusters that have been proposed to host SN Plio: the $\sim$50 pc location of the Tucana–Horologium (Tuc–Hor) association and the $\sim$100 pc distance to the Scorpius–Centaurus (Sco–Cen) association. We see that the clustered data points are consistent with the Tuc–Hor distance, though a somewhat larger $f_{60} \times M_{ej,60}$ would favor Sco–Cen. Finally, we note that the maximum size of an SNR can be estimated from the "fadeaway distance" (Draine 2011) when the blast wave becomes a sound wave, which depends on the density of the ambient medium but is $\sim$100–150 pc. We see that all of the points are inside this

distance, as would be expected for a supernova origin of ^{60}Fe— except for L16. Thus, aside from L16, the ^{60}Fe data are consistent with astrophysical expectations, which represents a nontrivial test, because astrophysical distances are not built into the ^{60}Fe measurements (in contrast to the of order megayear timescale that is preordained by the choice of ^{60}Fe).

We now examine the data sets and results in Figure 1 in more detail. There are three possible uptake factors to use for the K04 data (see Section 3.1 and Table 1) and all three have been included as separate date points to demonstrate the effect

of the uptake factor on the supernova distance. The F08 data have two points to represent the two options presented in Table 4 of F08; these are the same sediment sample fluence calculated two different ways, not independent measurements (see Section 3.2). The uptake factors for the W16 and W21 crusts and nodules are calculated based on the assumption that the W16 sediment collected 100% of the ^{60}Fe fluence, and so all of the W16 and W21 data are correlated and trace approximately the same distance (see Section 3.4). The K04 point with $U_{60} = 0.04$ (orange cross in Figure 1) is similarly calculated and therefore also correlated with the W16 and W21 data.

The F16 lunar data are plotted as a dashed line showing the full possible range quoted in F16. As described in Section 3.5, the time window for this fluence covers the last 8 Myr, during which there have been two near-Earth supernovae at 3 and 7 Mya. However, the 3 Mya supernova contributes 90% of the observed fluence (as calculated in Section 3.5.1) and therefore the dashed line more or less traces the available distance and fluence range for SN Plio.

It is of note that the W16 sediment fluence and the two possible F08 fluences fall on the lunar fluence line, with the significantly more precise W16 sediment in exact agreement. The full implications of this alignment are analyzed in Section 3.5, but altogether it does lend credence to the idea that the deep-sea sediments are sampling 100% of the ^{60}Fe flux which falls on the Earth.

3.1. Knie et al. (2004; K04) Data

The K04 FeMn crust was the first measurement of the ^{60}Fe signal from SN Plio that provided a time profile. Since the paper was published, the ^{60}Fe and ^{10}Be half-lives have been updated: the ^{60}Fe half-life has changed from 1.47 Myr (Kutschera et al. 1984) to 2.62 Myr (Rugel et al. 2009; Wallner et al. 2015; Ostdiek et al. 2017), while the ^{10}Be half-life has changed from 1.5 to 1.36 Myr (Nishiizumi et al. 2007) to 1.387 Myr (Korschinek et al. 2010). W16 update K04's fluence for these half-life changes in their Table 3 and we use those numbers here. It should be noted that the same FeMn crust was measured by F08, who confirmed the ^{60}Fe signal results.

FeMn crusts do not absorb all of the available iron in the seawater they contact; thus, it is necessary to calculate an uptake efficiency factor, U_{60}, for the crust. Unfortunately, this factor cannot be measured directly and must be inferred. K04 cite Bibron et al. (1974) as a means of calculating the uptake factor for the FeMn crust. By using the known ^{53}Mn extraterrestrial infall and comparing elemental ratios of Mn and Fe in seawater to the ^{53}Mn found in the FeMn crust, K04 were able to estimate the Fe uptake factor. As explained in F16 and confirmed by T. Faestermann and G. Korschinek (private communication), recent work with the ^{53}Mn infall corrects the values of Bibron et al. (1974) by a factor of 40 smaller. The factor of 40 decrease in ^{53}Mn leads to a relative factor of 40 increase in ^{60}Fe to match the ^{60}Fe/^{53}Mn ratio detected in the crusts, and thus the ^{60}Fe uptake for the FeMn crust in K04 changes from 0.6% to 24%.

An alternative method to calculate the uptake factor for the crust is to use a known ^{60}Fe infall over the relevant period of time, such as the W16 sediment.[8] By dividing the K04

incorporation by the W16 sediment incorporation in Table 3 of W16, we find an uptake factor of 4%, consistent with the FeMn crust and nodule uptakes in W16 and W21, who use the same method. This method correlates all of the distance measurements that are based off of the W16 sediment, leaving only the F08, L16, and F16 values as independent measurements.

To demonstrate the importance of the uptake factor in the distance calculation, the three options for the K04 uptake ($U_{60} = 0.6\%$, $U_{60} = 4\%$, and $U_{60} = 24\%$) are shown in Table 1 and Figure 1.

3.2. Fitoussi et al. (2008; F08) Data

F08 measured ^{60}Fe in both FeMn crusts and in deep-sea sediments. They first repeated the ^{60}Fe analysis on the same crust as used by K04, confirming the ^{60}Fe peak; since that work recreates an existing measurement, we do not use those results in this paper. F08 also pioneered the first ^{60}Fe analysis on deep-sea sediment samples. They found no significant signal unless they binned their data using a running-means average of either 0.4 or 0.8 Myr, as shown in their Figure 4.

The theory at the time was that the ^{60}Fe was in dust following the supernova blast wave, which would take about 10 kyr to sweep over the solar system (Fry et al. 2015). The ^{60}Fe timescale they were looking for (to match the fluence seen in K04) was actually spread over $\gtrsim 1$ Myr (Ertel et al. 2023), as would be shown in later work such as by L16 and W16—thus greatly diluting the signal they expected to find. Although the F08 sediment data cannot be used for a reliable time profile, we are able to include it in this work, as we are interested in measuring the fluence of their data and not the specific timing details.

Using the two running-means averages shown in Figure 4 of F08, we calculate the area under the curve and thereby the fluence by fitting a triangle to the upper plot (A) and two back-to-back triangles to the lower plot (B). To find a fluence comparable to what is shown in other work, we (1) updated the ^{10}Be half-life from 3.6 to 3.87 Myr (Korschinek et al. 2010) and changed the timescale accordingly; (2) subtracted the background of 2.3×10^{-16} from the ^{60}Fe/Fe ratio; and (3) decay corrected the ^{60}Fe/Fe ratio using $t_{1/2} = 2.62$ Myr.

From there, we were able to calculate the fluence for F08 via

$$\mathcal{F}_{\text{obs}} = \int \frac{^{60}\text{Fe}}{\text{Fe}} \, \rho \, \dot{h} \, c_{\text{Fe}} \, dt, \qquad (4)$$

where $\rho = 1.6$ g cm^{-3} is the sediment density, $\dot{h} = 3000$ cm Myr^{-1} is the sedimentation rate, and $c_{\text{Fe}} = 5.39 \times 10^{19}$ atoms g^{-1} is the iron concentration in the sediment, corresponding to a mass fraction of 0.5 wt%. Errors were pulled from the 1σ lines around the running averages in Figures 4(a) and (b) of F08. The results are shown in Table 1, labeled A and B to match the relevant plots in the original paper.

3.3. Ludwig et al. (2016; L16) Data

The L16 sediment data are notable in that the group set out to answer a different research question than the other ^{60}Fe analyses: instead of measuring the total ^{60}Fe over a specific time range, their goal was to prove that the iron was not moving around in the sediment column due to chemical processes. To achieve this, they focused on analyzing microfossils in the sediment and discarded iron material $\gtrsim 0.1$ μm, using the assumption that, since the ^{60}Fe is vaporized on impact with the atmosphere, there

---

[8] This method was not available for the original calculation, as ^{60}Fe would not be measured in sediments until F08.

should not be any ^{60}Fe in larger sized grains. However, the resulting $\mathcal{F}_{obs}$ is notably 1–2 orders of magnitude smaller than the other deep-sea sediments measured in F08 and W16, as well as the range for the lunar fluence in F16. As can be seen in Table 1, the low $\mathcal{F}_{obs}$ in L16 puts SN Plio at an implausibly far distance from Earth, bringing into question whether dust from a supernova at that distance can even reach our solar system (Fry et al. 2015, 2020). It is possible to manipulate the values for the dust fraction and ejected mass used in the distance calculation to bring the supernova predicted with the L16 sediment fluence to within a reasonable distance of Earth (i.e.,: to within at most 150–200 pc away, see Sections 4.2 and 4.1). Unfortunately, doing so pushes the rest of the observed ^{60}Fe fluences within the 10 pc "lethal distance" and is therefore not realistic.

L16 compare their data to the sediment fluence found in W16 and attribute the difference to global atmospheric fallout variations. However, as noted in Fry et al. (2015) and Ertel et al. (2023), latitude variations would account for a factor of 5 difference at the most—this is not enough to offset the differences in the observed fluences. Furthermore, the sediment samples from F08 and W16 see similar fluences despite significant location differences (off the coasts of Iceland and Australia, respectively). It should also be noted that, while latitude fallout variations may account for some range in $\mathcal{F}_{obs}$, the supernova origin should be within 200 pc in order for its debris to reach Earth. Therefore, we must assume that some of the discarded sample from L16 contained ^{60}Fe.

The work of L16 conclusively demonstrated that the ^{60}Fe is not moving within the sediment column after being deposited. This is a major contribution to the field, considering that the observed ^{60}Fe data are spread over an order of magnitude longer timescale than what is conventional for a supernova shock wave and there are considerable implications for this effect to be astronomical in origin rather than geophysical (Ertel et al. 2023). However, due to the fact that the ^{60}Fe fluence results in a >400 pc supernova distance, we will not be using the numbers from L16 in this study.

3.4. Wallner et al. (2016; W16) and Wallner et al. (2021; W21) Data

W16 measured the 3 Mya ^{60}Fe signal in two FeMn crusts, two FeMn nodules, and four deep-sea sediments. They greatly increased the known evidence of the signal and were also able to find indications of a second ^{60}Fe signal at 7 Mya. W21 followed up these measurements in a separate FeMn crust and were able to verify the 7 Mya supernova signal as well as provide an excellent time profile of both supernovae.[9]

W16 and W21 calculated the uptake factors for their FeMn crusts and nodules by assuming that their sediment samples observed 100% of the flux of ^{60}Fe onto Earth.[10] This connection between the different data sets means the resulting distance numbers are entirely correlated—as seen in Table 1 and Figure 1, the W16 and W21 data trace the same supernova

distance. When using the K04 uptake as 4% based off the W16 sediment, the K04 data are similarly correlated.

It should be noted that W16 and W21 quote "deposition rate" and "incorporation rate," respectively, instead of a fluence. This is the fluence into the material, which we use throughout this paper. To connect it to the fluence into the solar system that is quoted later in W16 and W21, factors such as uptake and global surface area must be accounted for and corrected out of the equation.

W21 measured the ^{60}Fe in an FeMn crust from 0 to 10 Mya using sample slices of ~400 kyr. In doing so, they created a detailed time profile showing two ^{60}Fe peaks in the last 10 Myr, which can be attributed to two supernovae. The peaks were measured in the same sample using the same analytical techniques—thus if we compare their relative fluences, most of the geophysical complications and systematic errors drop out of the results. Only issues such as fluctuations in the growth rate over millions of years and other large shifts in absorption into the crust over long periods of time will influence the results.

3.5. Fimiani et al. (2016; F16) Data

Unlike the Earth-based samples, the lunar samples analyzed by F16 are not affected by atmospheric, geologic, or biologic processes. They also present an analysis that is fully independent from anything measured on Earth and which can be used to verify the many different techniques and sample types involved in analyzing the ^{60}Fe signals.

When using the lunar data, we must work with two effects caused by the lack of atmosphere: cosmic-ray nucleosynthesis and micrometeorite impacts. The solar and Galactic cosmic rays create a natural background of ^{60}Fe in the lunar regolith and any ^{60}Fe signal related to SN Plio will be shown in an excess of ^{60}Fe above the standard background. In addition, the micrometeorite impacts create a "lunar gardening" effect that churns the top regolith and makes time resolution under 10 Myr ambiguous (F16; Costello et al. 2018). In previous work, gardening was not an issue, as the excess ^{60}Fe in the ~8 Myr sample was attributed to SN Plio; however, W21 have shown that there are actually two near-Earth supernovae in the last 10 Myr, at 3 and 7 Mya. Therefore, the excess ^{60}Fe in the lunar regolith accounts for both supernovae, and in order to accurately calculate the distance to SN Plio using the lunar data, we first need to portion the excess ^{60}Fe signal between the two supernovae.

3.5.1. Data-driven Portioning with the W21 Results

With the data from W21, we have an ^{60}Fe signal that goes back 8 Myr and shows two distinct supernova peaks. By taking the fluence ratio of these peaks, we are able to portion the lunar ^{60}Fe signal into two separate supernovae. W21 has the ^{60}Fe fluence for SN Plio (3.1 Mya) $\mathcal{F}_{obs} = 6.10 \times 10^6$ atoms cm^{-2} and for SN Mio (7.0 Mya) $\mathcal{F}_{obs} = 1.77 \times 10^6$ atoms cm^{-2}, both of which are decay corrected.[11] The F16 lunar data are also decay corrected, under the assumption that the excess ^{60}Fe

---

[9] W21 note that the observed time profile in the crust is wider than anticipated for SN Plio (which is profiled in the W16 sediments), indicating that factors such as crust porosity could affect these results.

[10] Koll et al. (2019) and Wallner et al. (2020) both study the current low-level ^{60}Fe infall, found in Antarctic snow and the top layers of the W16 sediments, respectively. Both groups find approximately the same current flux of ^{60}Fe— considering that these are very different sample types in different environments and global locations, this could be used as strong evidence that the 100% uptake assumption for deep-sea sediments is accurate, and that the W16 sediment data do accurately express the global ^{60}Fe fallout for SN Plio.

[11] W21 quotes an "incorporation rate," which is proportional to the fluence; however, we are only interested in the ratio between these two values and thus the difference falls out. Furthermore, since the two supernova peaks were measured in the same data slice from the same FeMn crust, the systematic and geo-related errors (such as uptake factor, various Earth processes that affect the signal, and any errors with absolute timing) cancel out.
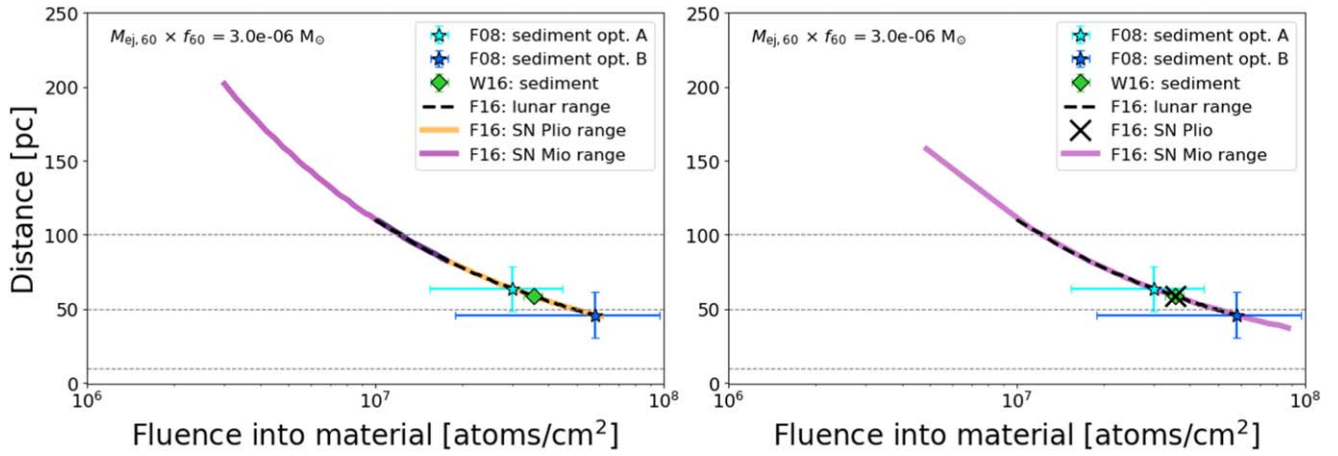
Figure 2. Lunar fluence portioning. Left: lunar fluence portioned with the W21 fluence ratios (see Section 3.5.1), along with the F16 published full lunar range. SN Plio (3.1 Mya) is in gold and SN Mio (7 Mya) is in purple; note the overlap. SN Plio is responsible for 90% of the lunar ^{60}Fe and therefore traces nearly the same range as the originally published data (dashed line). Right: lunar fluence portioned assuming the W16 sediment data are the full fluence for SN Plio (see Section 3.5.2). The SN Plio fluence is plotted with a black X, directly on top of the W16 sediment point. The purple line shows the possible remaining fluence and distance range for SN Mio, along with the original lunar data as a dashed line. Included on both plots for demonstration are the F08 and W16 sediment data.

signal seen in the 8 Myr sample was actually deposited 2.6 Mya (to match the K04 FeMn crust signal). We now know that two supernovae occurred within the last 8 Myr and therefore this decay correction needs to be fixed.

To portion the lunar signal, the first step is to undo the decay correction on all three fluences using

$$\mathcal{F}_0 = \mathcal{F}\, 2^{-t_{\mathrm{arr}}/t_{1/2}}, \qquad (5)$$

where $\mathcal{F}_0$ is the "dug up" fluence, $\mathcal{F}$ is the decay-corrected fluence, t_{arr} is the time that was used to decay correct the fluence (which in this case is the expected arrival time of the ^{60}Fe signal), and $t_{1/2}$ is the half-life of the isotope (2.62 Myr for ^{60}Fe). $t_{\mathrm{arr}} = 2.6$ Myr for the lunar signal in F16 and $t_{\mathrm{arr}} = 3.1$ and 7.0 Mya for the two W21 crust signals corresponding to SN Plio and SN Mio. From there, we can calculate the respective ratio of the two supernovae fluences to each other, with

$$\mathcal{P}_{\mathrm{Plio}} = \frac{1}{(\mathcal{F}_{\mathrm{Mio}}/\mathcal{F}_{\mathrm{Plio}}) + 1}, \qquad (6)$$

$$\mathcal{P}_{\mathrm{Mio}} = 1 - \mathcal{P}_{\mathrm{Plio}} = \frac{\mathcal{F}_{\mathrm{Mio}}}{\mathcal{F}_{\mathrm{Plio}}}\,\mathcal{P}_{\mathrm{Plio}}, \qquad (7)$$

where $\mathcal{P}_{\mathrm{Plio}}$ and $\mathcal{P}_{\mathrm{Mio}}$ are the percentages of the fluence from each supernova. We find that about 90% of the excess lunar ^{60}Fe signal should come from SN Plio (3.1 Mya), and 10% should come from SN Mio (7.0 Mya). We can then portion the "dug up" lunar fluence range of $1\text{–}6 \times 10^6$ atoms cm^{-2} and redo the decay correction, using $t_{\mathrm{arr}} = 3.1$ Myr for SN Plio and $t_{\mathrm{arr}} = 7.0$ Myr for SN Mio (W21). From there, we can calculate the distances to the two supernovae using Equation (2). It should be noted that this calculation assumes the same $M_{\mathrm{ej,60}}$, f_{60}, and travel time for both supernovae; these values, possible ranges, and effects on the distance are examined in detail in Sections 4 and 5.

Using $M_{\mathrm{ej,60}} = 3.0 \times 10^{-5}\ M_\odot$, $f_{60} = 0.1$, and $t_{\mathrm{trav}} = 0.1$ Myr, we find that SN Plio occurred between 45 and 110 pc from Earth and SN Mio occurred between 80 and 200 pc. The left plot in Figure 2 shows these two ranges in gold and purple, respectively, along with the original lunar range quoted in F16.

Note that the lunar fluence for SN Plio is about 10% less than the total lunar fluence for the last 8 Myr quoted in F16; the 10% loss results in a distance that is only a few parsecs different, meaning that a 10% difference in the fluence does not have a large impact on the distance calculation. However, this difference does allow us to extract additional information about the distance to the second supernova.

The full range of the lunar fluence corresponds to a distance range for SN Plio from 45 to 110 pc. It is interesting to note that the W16 sediment data (assumed to have a 100% uptake factor) fall exactly on this band and the two possibilities for the F08 sediment data include the band within the errors. These are completely independent measurements and in fact occur on separate bodies in the solar system. An extension of this work is to use the W16 sediment fluence and calculated distance to pinpoint what the actual lunar fluence is for SN Plio, with the remainder of the excess ^{60}Fe then originating from SN Mio, which we do below.

3.5.2. Data-driven Portioning with the W16 Results

As noted in the previous section, the W16 sediment fluence falls exactly in the range of the lunar fluence. In this section, we make the assumption that the W16 sediment *is* the fluence from SN Plio at 3 Mya; therefore, any remaining lunar ^{60}Fe fluence detected is from SN Mio at 7 Mya. Once again undoing the decay correction on the lunar fluence and the W16 sediment fluence with Equation (5), we can subtract the "dug up" W16 fluence from the lunar fluence, redo the 7 Mya decay correction, and recalculate the possible distance range to SN Mio with Equation (2). Using the same astrophysical parameters ($M_{\mathrm{ej,60}} = 3.0 \times 10^{-5}\ M_\odot$, $f_{60} = 0.1$, and $t_{\mathrm{trav}} = 0.1$ Myr), we find that the SN Mio distance range with this method is 40–160 pc.

The right plot in Figure 2 shows the results of this calculation. The fluence from SN Plio is denoted with a black X and is plotted directly over the W16 sediment fluence (as these are the same number). The shaded purple line represents the full possible range of fluence and distance for SN Mio, with the original F16 range plotted as a black dashed line.

Parameter		Range
Ejected ^{60}Fe mass, $M_{\mathrm{ej},60}$	$[M_\odot]$	3×10^{-6}–3×10^{-4}
Dust fraction, f_{60}		1%–100%
Travel time, t_{trav}	[Myr]	0.1–1.5

4. Models

The ^{60}Fe signal found in the natural archives on Earth can be used to find the $\mathcal{F}_{\mathrm{obs}}$, t_{arr}, and U_{60} parameters needed to calculate the supernova distance in Equation (2). For the remaining three parameters of $M_{\mathrm{ej},60}$, f_{60}, and t_{trav}, we turn to astrophysical models and observations to provide additional constraints, and we explore the allowed ranges that remain. A brief summary of the parameter ranges are listed in Table 2 and these ranges are discussed in detail in the following subsections.

4.1. Ejected Mass

There are no available measurements of ^{60}Fe yields in individual supernovae. Thus we have two options. One is to rely on theoretical predictions. The other is to use observations of ^{60}Fe gamma-ray emission from the Galaxy to find an average ^{60}Fe yield. We consider each of these in turn.

4.1.1. Supernova Calculations of ^{60}Fe Yields

Finding the ejected mass of ^{60}Fe from a supernova requires modeling explosive nucleosynthesis in the shell layers of the progenitor as it explodes. The ^{60}Fe is not made in the core of the CCSN but instead from neutron capture onto preexisting iron in the shell layers (for a recent review, see Diehl et al. 2021). For this reason, we exclude explosion models with low metallicity or which do not track nucleosynthesis in the shell layers, such as the Curtis et al. (2019) "s model" and the Wanajo et al. (2018) "s models."

There are some additional constraints we can place on the available nucleosynthesis models. As discussed in Fry et al. (2015), the supernova must be a CCSN or ECSN in order to produce sufficient ^{60}Fe. It must also be close enough to Earth for its debris to reach the solar system. While we have already excluded models with low metallicity, which will not make ^{60}Fe, the progenitor should already be at or near solar metallicity due to its proximity to Earth and the time of the explosion ($\lesssim 10$ Mya).

Table 3 highlights the relevant simulation parameters for the selected models. We focus on four recent publications which model stars of solar metallicity and include ^{60}Fe production in their nucleosynthesis reactions (Sukhbold et al. 2016; Limongi & Chieffi 2018; Wanajo et al. 2018; Curtis et al. 2019). Rauscher et al. (2002) is included to enable comparison with the data used in Fry et al. (2015). Figure 3 then plots the ^{60}Fe yields from the five different groups, with each individual model plotted separately. Lines connect the individual masses to give a better sense of the model's range; the single point from Wanajo et al. (2018) focuses on a specific mass ECSN model.

The focus of this paper is not to describe these supernova models in detail, but instead to find a range of the ejected mass of ^{60}Fe that can be used in Equation (2). From Figure 3, we see that the possible range extends from 3×10^{-6} to 3×10^{-4} $M_\odot$ and is covered fairly evenly by all groups. A recent further discussion of ^{60}Fe production in supernovae appears in Diehl et al. (2021).

Figure 4 shows the radioactivity distance implied by these yields. Here we adopt the ^{60}Fe fluence from W16 sediments, along with a dust fraction $f_{60} = 0.1$. We see that the wide range of yields in Figure 3 leads to a substantial range in the radioactivity distance, even with the $M_{\mathrm{ej},60}^{1/2}$ scaling. Encouragingly, we see that almost all models give distance between the lethal and fadeaway limits. This represents a nontrivial success of the nearby supernova scenario, because calculation of D in Equation (2) depends only on the fluence measurements and yields, with no astrophysical distances built in. Moreover, the allowed distance range encompasses the Local Bubble, and star clusters proposed to be the sites of the supernovae, as discussed below in Section 6.

While Figure 4 shows the full range of masses for which ^{60}Fe is presented in recent models, these stars are not all equally probable. The stellar initial mass function shape indicated that lower-mass CCSN progenitors should be common; here we see that across several models these all provide reasonable distances. Indeed we do not see clear systematic differences between the distances inferred with lower- versus higher-mass models, reflecting the lack of a clear trend in ^{60}Fe yields versus progenitor mass in Figure 3. This suggests that it will be difficult or impossible to use ^{60}Fe alone to probe the mass of the progenitor; for this multiple supernova radioisotopes are needed.

We stress that the distances shown in Figure 4 derive from the dust fraction choice $f_{60} = 0.1$, and scale as $D \propto f_{60}^{1/2}$. Thus, significant systematic changes in D can result from different choices for this poorly determined parameter. This point is discussed further in the following section.

With this caveat in mind, it is notable that Figure 4 also shows that a few ^{60}Fe calculations do not fall into the allowed range. Most notable are the Limongi & Chieffi (2018) models, which give $D \approx 0$ for progenitor masses $\geqslant 30$ $M_\odot$. This arises because in these models there is a direct collapse to a black hole without an explosion and the accompanying ejection of nucleosynthesis product; thus the only ^{60}Fe that escapes is the small amount in the stellar wind. Clearly these models are excluded, but the lower-mass models of Limongi & Chieffi (2018) give ^{60}Fe in good agreement with other calculations and thus give a plausible radioactivity distance.

Finally, we note that Figure 4 updates a similar calculation by Fry et al. (2015, their Figure 3). Our results are broadly similar. This agreement is somewhat accidental, since those earlier results were based on K04 and F08 ^{60}Fe crust measurements prior to the more reliable sediment measurement of W16 (used in this work). Moreover, the uptake and dust assumptions were different. On the other hand, while detailed stellar yields have changed, they continue to span a similar range.

4.1.2. The Average ^{60}Fe Yield from Gamma-Ray Line Observations

Gamma-ray line astronomy provides an estimate of the average ^{60}Fe yield from supernovae. The radioactive decay of ^{60}Fe atoms leads to the emission of gamma-ray and X-ray lines. Interstellar ^{60}Fe thus produces observable gamma-ray lines that probe its production over approximately one ^{60}Fe lifetime.

Measurements of diffuse Galactic gamma rays give a steady-state ^{60}Fe mass of $M_{60,\mathrm{SS}} = 2.9^{+2.2}_{-0.78}$ $M_\odot$ (Diehl et al. 2021). In steady state, $M_{60,\mathrm{SS}} = \langle M_{\mathrm{ej},60} \rangle \, \tau_{60} \, \mathcal{R}_{\mathrm{CCSN}}$, where $\mathcal{R}_{\mathrm{CCSN}} = 1.79 \pm 0.55$ century^{-1} is the present-day Galactic core-collapse rate (Rozwadowska et al. 2021). We thus find the mean ^{60}Fe

Table 3
Supernova ^{60}Fe Yield Models

Authors	Model	Metallicity	Rotation	Mass Range ($M_\odot$)	Type
Rauscher et al. (2002)	⋯	solar	no	12–25	CCSN
Sukhbold et al. (2016)	N60	one-third solar	no	12.25–120	CCSN
Sukhbold et al. (2016)	W18	one-third solar	yes	12.25–120	CCSN
Limongi & Chieffi (2018)	v0	solar	no	13–120	CCSN
Limongi & Chieffi (2018)	v150	solar	yes	13–120	CCSN
Limongi & Chieffi (2018)	v300	solar	yes	13–120	CCSN
Wanajo et al. (2018)[a]	e8.8	solar	no	8.8	ECSN
Curtis et al. (2019)	w	solar	no	12–120	CCSN

Note.
[a] The e8.8 model used in Wanajo et al. (2018) is the same as used in Wanajo et al. (2013).

yield to be

$$\langle M_{\mathrm{ej},60}\rangle = \frac{M_{60,\mathrm{SS}}}{\tau_{60}\,\mathcal{R}_{\mathrm{SN}}}$$

$$= 4^{+4}_{-2} \times 10^{-5} M_\odot \left(\frac{M_{60,\mathrm{SS}}}{2.85\,M_\odot}\right)\left(\frac{1.79\text{ event/century}}{\mathcal{R}_{\mathrm{SN}}}\right). \quad (8)$$

This result averages over all CCSNe, which are assumed to be the only important ^{60}Fe source. If another source such as AGB stars makes an important contribution to the Galactic ^{60}Fe inventory, then the mean supernova yield would be lower.

Interestingly, the result in Equation (8) is in the heart of the predictions shown in Figure 3. This supports the idea that CCSNe indeed dominate ^{60}Fe production, and suggests that the theoretical predictions are in the right ballpark. Further, if this is a typical yield, then there are implications for the dust fraction, to which we now turn.

4.2. Dust Fraction

Our current understanding of the interactions between the supernova shock front and the heliosphere require the ^{60}Fe to be in the form of dust grains in order to reach Earth (Benítez et al. 2002; Athanassiadou & Fields 2011; Fry et al. 2015, 2016). The heliosphere blocks the supernova shock front from pushing inward past 5 au for supernova distances > 30 pc (Miller & Fields 2022), and therefore only dust grains $\gtrsim 0.1$ μm can ballistically push through the barrier (Athanassiadou & Fields 2011; Fry et al. 2020). The dust fraction parameter f_{60} describes the fraction of ejected ^{60}Fe mass which condenses into dust and therefore makes it to Earth—this parameter encompasses the multiple boundaries and survivability filters that the dust must traverse. As laid out in Fry et al. (2015) Table 3, these include:

1. the amount of ^{60}Fe that initially forms into dust;
2. the amount of ^{60}Fe-bearing dust which survives the reverse shock, sputtering, collisions, and drag forces in the SNR to then encounter the heliosphere;
3. the amount of dust that makes it past the shock–shock collision at the heliosphere boundary; and
4. the amount of dust which manages to traverse the solar system to 1 au and be collected on Earth (and the Moon).

Observational work on SN 1987A has demonstrated refractory elements form dust within years of the explosion and that nearly 100% of supernova-produced elemental iron condenses immediately into dust (Matsuura et al. 2011, 2017, 2019; Dwek & Arendt 2015; Cigan et al. 2019). The composition of ^{60}Fe-bearing dust is of specific interest, especially considering that different compositions have significantly different survival rates due to grain sputtering (Silvia et al. 2010, 2012; Fry et al. 2015). Given that the ^{60}Fe is formed in the shell layers of the progenitor and not in the iron core with the bulk of the supernova-produced elemental iron (Diehl et al. 2021), it is quite possible that the ^{60}Fe dust is not in predominately metallic iron grains—this in turn can affect the dust's survival chances (Silvia et al. 2010).

The degree to which dust is produced and destroyed within SNRs is an area of ongoing research; a recent review by Micelotta et al. (2018) summarizes the current theory and observational work. CCSNe are producers of dust, as shown by observations of grain emission in young remnants, e.g., in recent JWST observations (Shahbandeh et al. 2023). The portion of grains that survive and escape the remnant is more difficult to establish. Factors such as dust composition, size, clumpiness within the remnant, and the density of the ambient medium all impact the dust survival rate. Table 2 in Micelotta et al. (2018) lists the calculated dust survival fractions within the SNR for various models and simulations. These dust fractions vary wildly between models and ultimately range from 0% to 100% of the supernova-produced dust surviving the forward and reverse shocks. More recent papers continue to find that a large range is possible (Marassi et al. 2019; Slavin et al. 2020).

There are many dynamics and effects within the solar system which can filter dust grain sizes and prevent grains from easily entering the inner solar system (Altobelli et al. 2005; Mann 2010; Altobelli et al. 2016; W16; Strub et al. 2019); however, the $\sim$100 km s^{-1} speed at which the supernova-produced dust is traveling causes these effects to be negligible (Athanassiadou & Fields 2011; Fry et al. 2015). Therefore, we will consider the dust fraction at Earth's orbit to be equal to the surviving dust fraction within the SNR. Note that this assumption is in contrast to the assumptions made in Table 2 in Fry et al. (2015), who assume that only 10% of the metallic iron (Fe) dust and none of the troilite (FeS) dust cross the heliosphere boundary.[12]

---

[12] Upon closer examination of the sources cited (Linde & Gombosi 2000; Silvia et al. 2010; Slavin et al. 2010), we find that they are focused on ISM grains which are traveling $\sim$26 km s^{-1}; our SNR grains are traveling at $\sim$100 km s^{-1}. Further research is needed to work out the details of the dust's ability to penetrate the heliosphere depending on size and velocity—for the purpose of this paper, we follow the approach outlined in W16.
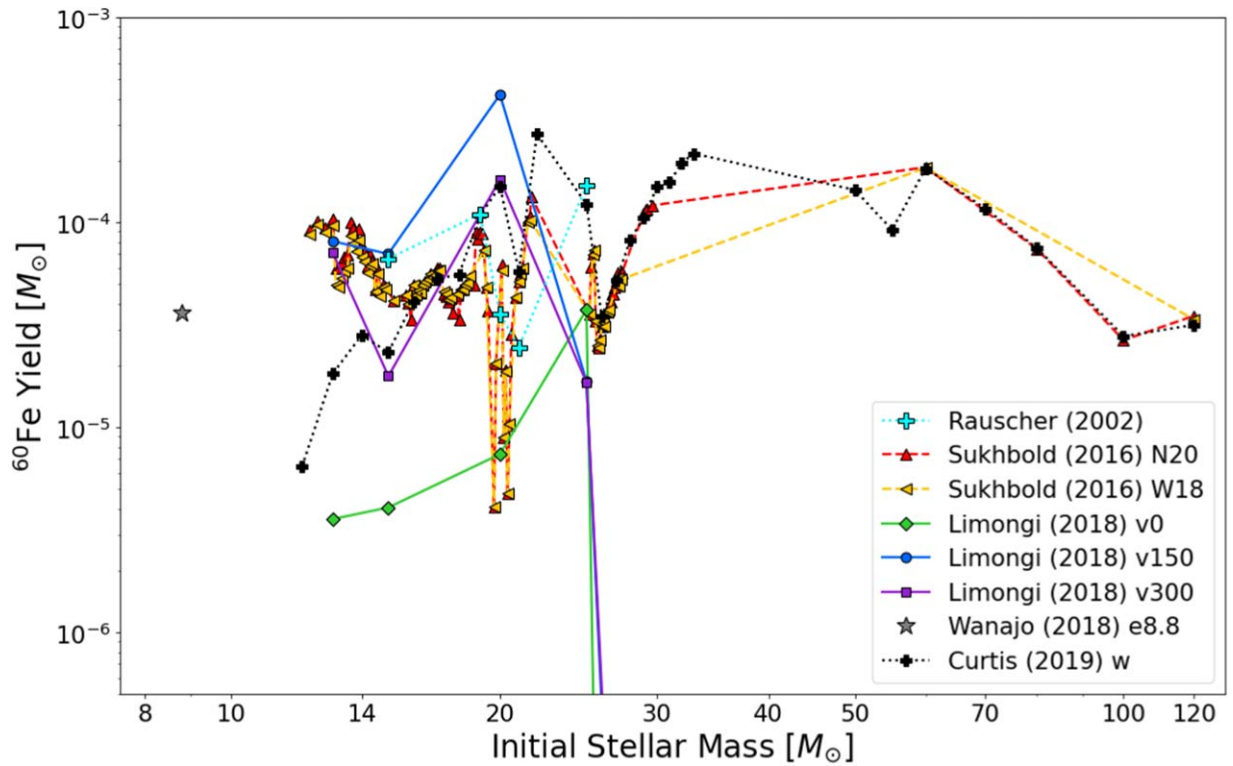
Figure 3. Supernova model yields for ^{60}Fe. Masses within models are connected with lines. Note that the possible ranges for $M_{\mathrm{ej},60}$ vary between about 3×10^{-6} and 3×10^{-4} $M_\odot$. The three Limongi & Chieffi (2018) models drop off the plot and demonstrate direct collapse to a black hole. The relevant paper citations and details can be found in Table 3.

In contrast, W16 follows a similar route to our approach in this paper, in assuming that the ^{60}Fe dust survives from the shock boundary to the Earth essentially unchanged.

With the assumptions that 100% of the ejected mass of ^{60}Fe condenses into dust and that the dust survives the heliosphere boundary fully intact, the main source of dust loss is within the SNR itself. As discussed above, the fraction of dust that survives the SNR environment ranges wildly depending on the model parameters such as size, composition, and ambient environment—although at least some of the dust must survive this journey, as we find the ^{60}Fe signal on Earth. For the purposes of this work, we do not focus on the details of the dust survival calculations but instead choose a general dust fraction of between 1% and 100%.

It should be noted that W16 and W21 calculate the dust survival fraction using the fluence from the W16 sediment sample (which samples 100% of the ^{60}Fe flux onto Earth). They assume that the ^{60}Fe dust traverses the solar system essentially unchanged and therefore the ^{60}Fe fluence at Earth is the same as the interstellar fluence. W16 find a dust survival fraction of 0.4%–9%, using the additional assumptions that the source of the 3 Mya signal occurred somewhere between 50 and 120 pc from Earth and with an ejected mass of $M_{\mathrm{ej},60} \sim 9 \times 10^{-5}$ $M_\odot$.[13] We do not use these numbers directly in this work, as they are unavoidably correlated to the observed

fluence. Thus we see that our adopted benchmark value $f_{60} = 10\%$ lies comfortably within the large allowed range, but clearly more work is needed to understand this quantity better. Indeed, as W16 and W21 show and we will discuss below, ^{60}Fe observations place novel limits on dust survival.

4.3. Travel Time

The travel time parameter (t_{trav}) is defined as how long the supernova dust containing the ^{60}Fe will travel within the remnant before reaching Earth—specifically, it is the dust's travel time before the start of the ^{60}Fe signal.[14] As the remnant expands, it cools and slows, achieving a maximum size of around 100–200 pc (Fry et al. 2015; Micelotta et al. 2018). At most, this expansion should last around 1–2 Myr (see Figure 1 in Micelotta et al. 2018). We therefore consider the range for t_{trav} to be 0.1–1.5 Myr. Note that any value of t_{trav} less than the half-life of ^{60}Fe ($t_{1/2} = 2.62$ Myr) has little to no impact on the resulting distance calculated.

It should be noted that at least SN Plio exploded in the Local Bubble environment and not the general ISM (see Zucker et al. 2022, for further discussion; see also Section 6.2). The low density does not change our estimate of t_{trav}: while the low density allows the remnant to expand farther, the blast also travels faster and therefore this extra distance is negligible.

There are also additional constraints due to the fact that we have observed an ^{60}Fe signal on Earth twice in the last 10 Myr. The dust containing ^{60}Fe arrived on Earth approximately 3 Mya

---

[13] This $M_{\mathrm{ej},60}$ value is found by assuming the supernova signal at 3 Mya is the debris from three separate supernovae, given the long >1 Myr infall timescale (similar to what is proposed in Breitschwerdt et al. 2016). As discussed in Fry et al. (2020), Ertel et al. (2023), and Chaikin et al. (2022), more than one supernova is not required to produce the observed signal and therefore this might overestimate the ejected mass. However, the value is still well within the range of possible values for $M_{\mathrm{ej},60}$ for a single supernova, as seen in Section 4.1.

[14] The dust containing the ^{60}Fe will continue to rain down for $\gtrsim 1$ Myr after the initial deposition. We therefore define the travel time as tracing the SNR shock front and not the specific dust dynamics within the remnant that extend the signal.
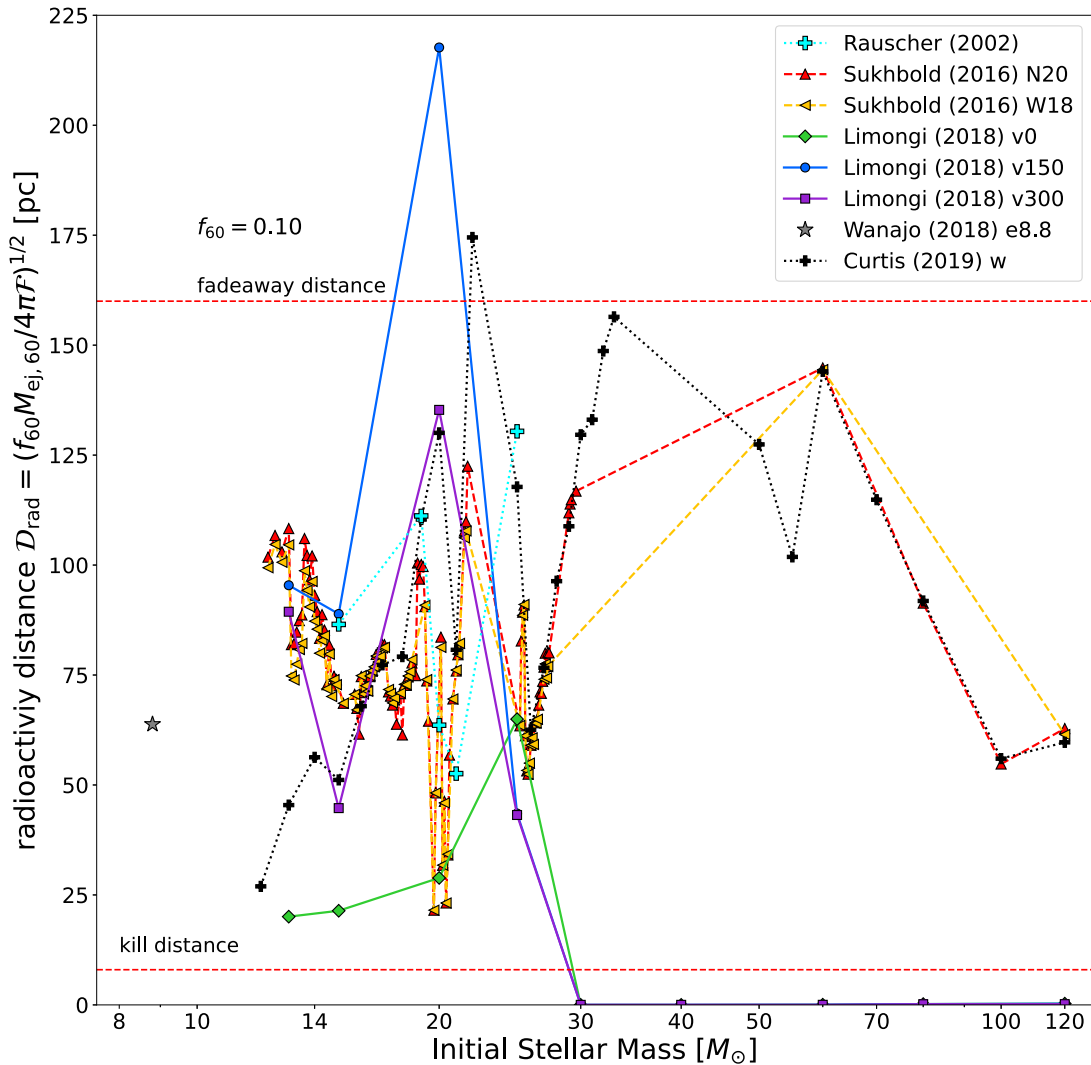
Figure 4. Radioactivity distance for the core-collapse ^{60}Fe yields shown in Figure 3. Results use the W16 sediment data and assume $f_{60} = 0.1$. Estimates of limiting distances are shown as dashed horizontal red lines: the lethal distance at 10 pc is a lower limit, and the fadeaway distance at 160 pc is an upper limit (Draine 2011). We see that for most models, the radioactivity distance lies between these limits, showing that a consistent picture is possible for this wide class of supernova models.

for SN Plio and 7 Mya for SN Mio. Our ability to detect the ^{60}Fe signal from that point is dependent on the half-life of ^{60}Fe. For SN Plio, we have lost about one half-life of the isotope since deposition, and about three half-lives for SN Mio. It is therefore reasonable to believe that the dust is not traveling for millions of years before reaching Earth, as a further loss of ^{60}Fe would imply either an enormous ^{60}Fe supernova production or raise questions over our ability to detect the ^{60}Fe signal at all.

5. Summary of Results

We combine the ranges of the three astronomical parameters discussed in Section 4 with the observed ^{60}Fe signal in Section 3 to calculate the full possible range of distances to SN Plio (3 Mya). Figure 5 maps out these results, following the same plotting convention of distance to supernova versus fluence into the material used in Figures 1 and 2. For each subplot, two of the parameters are held constant at a midrange value while the third is allowed to vary for the full range considered in this paper.

To reduce visual confusion, we have chosen to only show the F08 option A and the K04 crust with $U_{60} = 0.04$ points; using the K04 crust with $U_{60} = 0.04$ means that the F08 and

F16 distances are the only ones not correlated to the W16 sediment (see Section 3.1). As a reminder, the error bars on the fluence reflect the actual fluence errors—the error bars on the distance only trace the fluence errors and do not account for the error in U_{60} present on the FeMn crusts and nodules (see Section 3).

As can been seen in the bottom plot of Figure 5, the travel time does not have a large effect on the distance range and is the least important parameter. The difference between 0.1 and 1.0 Myr is negligible, on the order of ~5 pc, which is well within the uncertainties of the Earth-based parameters. It is only when the travel time is increased to a nonphysical 5 Myr that any effect is observed, and that effect is minimal compared to the ranges seen in the $M_{ej,60}$ and f_{60} parameters.

Both the dust fraction and ejected mass range 2 full orders of magnitude and have a significant influence on the distance. Untangling these parameters is challenging, and as discussed in Section 2, the product $f_{60} \times M_{ej,60}$ is more robust. Table 4 lists a range of possible $f_{60} \times M_{ej,60}$ values, covering the lowest and highest combinations, the middle of both ranges, as well as four distances of specific interest. All of the approximate distances in Table 4 are calculated using the W16 sediment fluence, as
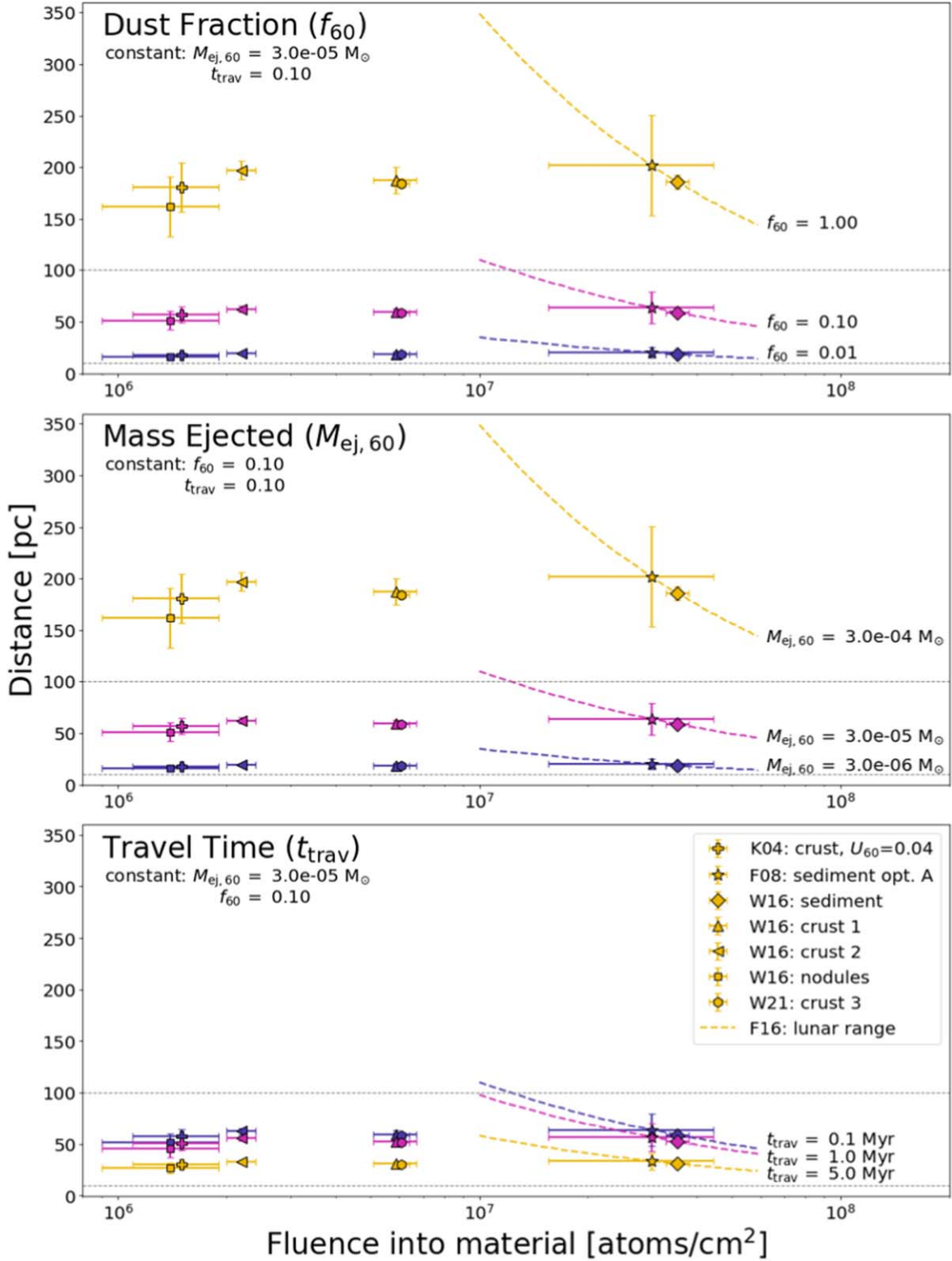
Figure 5. Effect of the three astrophysical parameters on the distance to SN Plio. For the purposes of reducing visual confusion, we only show the K04 distance calculated with $U_{60} = 0.04$ and the F08 option A points. Note that this means the F08 and F16 distances are the only ones not correlated to the W16 sediment. Top: dust fractions (f_{60}) of 1%, 10%, and 100%, holding the ejected mass and travel time constant. Middle: ejected masses ($M_{\rm ej,60}$) of 3.0×10^{-6} to $3.0 \times 10^{-4} \, M_{\odot}$, holding the dust fraction and travel time constant. Bottom: travel times ($t_{\rm trav}$) of 0.1, 1.0, and 5.0 Myr, holding the dust fraction and ejected mass constant. The dark blue, magenta, and yellow points for each plot indicate the distances calculated with the low, middle, and high values for each range, respectively. Lines have been drawn at 10 and 100 pc.

we believe this measurement best reflects the ^{60}Fe fluence from SN Plio (see Section 3.4 for further details).

Both the lowest and highest possible combinations of $M_{\rm ej,60}$ and f_{60} put SN Plio at implausible distances: any distance closer

than 20 pc should have left distinct biological damage tracers in the fossil record (Melott & Thomas 2011; Fields et al. 2020), while distances farther than ~160 pc prevent the dust from reaching Earth (Fry et al. 2015). The remaining combinations

Table 4
Influence of $f_{60} \times M_{ej,60}$ on SN Plio's Distance

$f_{60} \times M_{ej,60}$ ($M_\odot$)	Approximate Distance (pc)	Notes
3.0×10^{-8}	5.87 ± 0.22	lowest combination
8.85×10^{-8}	10	10 pc supernova
3.5×10^{-7}	20	20 pc supernova
2.18×10^{-6}	50	50 pc supernova
3.0×10^{-6}	59.7 ± 4.0	midrange
8.75×10^{-6}	100	100 pc supernova
3.0×10^{-4}	586 ± 22	highest combination

Note. $f_{60} \times M_{ej,60}$ ranges from the lowest combination ($M_{ej,60} = 3.0 \times 10^{-6} \, M_\odot$, $f_{60} = 1\%$) to the highest combination ($M_{ej,60} = 3.0 \times 10^{-4} \, M_\odot$, $f_{60} = 100\%$). $f_{60} \times M_{ej,60} = 3.0 \times 10^{-6} \, M_\odot$ reflects a mix of the highest and lowest parameter combination and also covers the midrange for both combinations. Specific distances of interest (10, 20, 50, and 100 pc) are also singled out. Distance is calculated using the W16 sediment fluence; the error on the distance reflects the observed fluence error.

produce a large range of possible supernova distances. Using an $f_{60} \times M_{ej,60}$ range of 5×10^{-7}–$5 \times 10^{-5} \, M_\odot$ yields distances between 20 and 100 pc; these values for $f_{60} \times M_{ej,60}$ can be found using any high–low or low–high combination of $M_{ej,60}$ and f_{60} as well as the middle range for both parameters.

In the interest of a complete analysis, we have expanded $M_{ej,60}$ and f_{60} to the full possible range of values—this does not necessarily reflect the most likely range. While the available ^{60}Fe yield models cover the full 3×10^{-6}–$3 \times 10^{-4} \, M_\odot$ for the mass range of interest (8–30 $M_\odot$), as seen in Figure 3, the dust fraction survival range is more likely to be between 1% and 50% (W16, W21; Slavin et al. 2020).

5.1. Distance to the 7 Mya Supernova

The W21 data set includes a distinct FeMn crust measurement for the 7 Mya supernova. We can use this fluence to calculate the distance to SN Mio following the same procedure as described for SN Plio. The fluence for SN Mio is $\mathcal{F} = 1.77 \pm 0.25 \times 10^6$ atoms cm^{-2}, with an uptake factor of $U_{60} = 17\%$ (W21)—the fluence is already decay corrected, so the arrival time is not needed. We assume the same average supernova properties as SN Plio, with $M_{ej,60} = 3.0 \times 10^{-5} \, M_\odot$ and $f_{60} = 0.1$, although these properties do not have to be the same for both supernovae. Using Equation (2), we find that the distance to SN Mio is

$$D(\text{SN Mio}) \simeq (108 \pm 8 \text{ pc.}) \left(\frac{f_{60}}{0.1} \right)^{1/2}$$
$$\times \left(\frac{M_{ej,60}}{3.0 \times 10^{-5} M_\odot} \right)^{1/2}, \qquad (9)$$

where the errors reflect only the reported uncertainties in the fluence. Calculating the distance using a ratio of the fluences found in W21 provides the same results, with $D_2 = D_1 \sqrt{\mathcal{F}_1/\mathcal{F}_2} \sim 110$ pc. Similarly, we note that the W21 crust 3 fluence (for SN Mio) and the distance calculated in Equation (9) fall exactly on the estimated range for SN Mio as shown in the lunar fluence (see Section 3.5.1)—this is unsurprising, as all three of these calculations are based off of the W21 crust fluences and are therefore correlated.
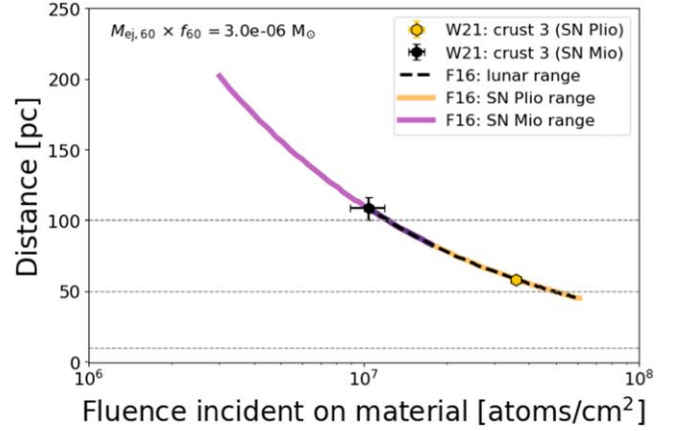

Figure 6. Distance to SN Mio. Plotted are the portioned lunar fluences with gold (SN Plio) and purple (SN Mio) lines (see Section 3.5.1 and Figure 2), the original lunar fluence with a black dashed line, the W21 crust 3 fluence for SN Plio in yellow, and the W21 crust 3 fluence for SN Mio in black. For ease of comparison, the W21 crust 3 measurements have been corrected for an uptake factor of 17%; they are therefore directly equivalent to the lunar measurements, which assume a 100% uptake. The distances to both SN Plio and SN Mio are calculated using the same $f_{60} \times M_{ej,60}$.

Figure 6 shows the distance to SN Mio compared to SN Plio. The distance calculated with the W21 crust 3 fluence for SN Mio is plotted along with the portioned lunar range corresponding to SN Mio. Two equivalent values are shown for SN Plio: the W21 crust 3 fluence for SN Plio and the portioned lunar range for SN Plio. To make the W21 crust 3 data directly comparable to the F16 lunar fluence, we have corrected for the 17% uptake factor in the crusts.[15]

We note that, given the available measurements, the fluence for SN Mio is around a factor of 2 smaller than the fluence for SN Plio. These values have been decay corrected and therefore this difference is real, excluding unknown geophysical parameters that could affect the signals. As discussed in Section 4, the influence this has on the calculated distance could be the result of a genuine difference in distance between the two supernovae or due to differences in the $f_{60} \times M_{ej,60}$ parameter; in reality, it is likely a combination of both scenarios.

Ideally, this calculation should be repeated with greater precision when there are more data available on SN Mio. With a detailed time profile, such as can be provided with sediment measurements, we might be able to investigate differences in the astronomical properties between the two supernovae; although as the above sections discuss there are significant ranges in such factors as the ^{60}Fe ejected mass and dust fraction, and differences in the supernovae distances could obscure these variations.

6. Discussion

Our results have an interplay with several areas of astrophysics, which we summarize here.

---

[15] As a reminder, the uptake factor accounts for how much of the ^{60}Fe fluence is lost between arrival at Earth and absorption into the sampled material. The lunar regolith, similar to the deep-sea sediments, has a 100% uptake factor, as it is assumed no fluence is lost. The W21 crust has a 17% uptake factor (see Section 3). Thus in Figure 6, we have accounted for the remaining 83% of the fluence in the crust measurements, to make them directly comparable to the lunar regolith measurements.

6.1. External Limits on Distance

As discussed in Section 5, it is difficult to limit the possible distance range to SN Plio from the astrophysical parameters alone. The theoretical values for both the ejected mass and dust fraction of ^{60}Fe individually cover 2 orders of magnitude and, although we can rule out a few of the most extreme combinations, we are unable to use them to put strong limits on the supernova distance. We therefore turn to other methods that can be used to provide limits.

Biological damage and extinctions. There has been a long history of speculating on the damage that supernova-driven cosmic rays could do to ozone in the atmosphere and implications for life on Earth (Shindewolf 1954; Shklovskii & Sagan 1966; Ruderman 1974; Benítez et al. 2002; Melott & Thomas 2011; Thomas et al. 2016). Gehrels et al. (2003) were the first to calculate that a distance of 8 pc would lead a factor of 2 UV enhancement due to ozone depletion. They argue that this represents a threshold for "significant biological effects," based on the work of Madronich et al. (1998), who among other things summarize evidence for enhanced DNA damage in Antarctica due to the human-created ozone hole and the resulting increase in UVB radiation.[16]

The study of Ejzak et al. (2007) argues that the key figure of merit for ozone destruction is the fluence (time-integrated flux) of ionizing radiation, and they argue for 100 kJ m^{-2} as a benchmark for lethal effects. Later updates by Fry et al. (2015) extend the distance for significant damage to 10 pc, which we have adopted in this paper as the "lethal distance" (see also Brunton et al. 2023), although recent work suggests that the distance could be as far as 20 pc (Thomas & Yelland 2023).

While more minor biological damage events and other climate-driven disruptions are still possible (Thomas 2018; Melott & Thomas 2019; Melott et al. 2019), we can also rule out any distance that would result in a mass extinction, as there are no major mass-extinction events 3 Mya.[17] This prevents the distance to SN Plio from being within 20 pc of Earth (Fields et al. 2020). Indeed, we note that in Figure 5, all of the distances derived from ^{60}Fe are larger than the lethal limit. From Table 4, we only fall below this limit by simultaneously making the most extreme choices of dust fraction f_{60} and ^{60}Fe yield $M_{ej,60}$. This serves as a consistency check.

Cosmic-ray distance calculation. There is a local ^{60}Fe component measured in cosmic rays, which is associated with a nearby supernova around 2 Mya (Binns et al. 2016). Kachelrieß et al. (2015, 2018) examine the proton, antiproton, and positron fluxes and anomalies in the cosmic-ray spectrum; they argue for a local source in addition to the contribution from cosmic-ray acceleration in SNRs throughout the Galaxy. Savchenko et al. (2015) show that a feature in the cosmic-ray anisotropy at 2–20 TeV is due to a single, recent, local event. Using these data they calculate a distance, estimating the source to be roughly 200 pc from Earth. It should be noted that while the ^{60}Fe cosmic-ray background is local and recent, these analysis relied on the detection of the ^{60}Fe signal for SN Plio—we now know of two supernovae which occurred in the last 10 Myr and

further analysis of the local cosmic-ray background will need to take this into account.

Nearby clusters. The massive stars that explode as CCSNe or ECSNe tend to form in clusters, most likely including the two near-Earth supernovae. We can use the locations of nearby stellar groups and associations as another method for constraining the supernova distances. The Tuc–Hor association is ∼60 pc from Earth (Mamajek 2015) and considered to be the mostly likely to host SN Plio (Fry et al. 2015; Hyde & Pecaut 2018).[18] Hyde & Pecaut (2018) surveyed the local associations and groups within 100 pc and concluded that Tuc–Hor is the only association with an initial mass function (IMF) large enough to host a CCSN, thus making it the most likely candidate.

Another consideration is the OB Sco–Cen association, favorable because it has the IMF to host multiple CCSNe and is likely the source of the supernovae which formed the Local Bubble (Frisch et al. 2011; Fry et al. 2015; Breitschwerdt et al. 2016). Sco–Cen is located around 130 pc from Earth (Fuchs et al. 2006) and this puts it at the farther edge of the possible distance range. Neuhäuser et al. (2020) even backtracked the positions of both a nearby pulsar and runaway star, claiming that they shared a common binary in proximity to Sco–Cen 1.78 Mya and could be the remnants of SN Plio— unfortunately, the timing does not quite work out for SN Plio, as the initial ^{60}Fe signal starts at 3 Mya and the progenitor of the signal must precede the deposition time.

Dust stopping time. Fry et al. (2020) simulate supernova-produced dust under the assumption that the dust is charged and will therefore be confined within the magnetized remnant. They find that their models can consistently propagate grains to 50 pc, but that greater distances are affected by magnetic fields and drag forces and unlikely to be reached. Although further research is needed, this work provides an interesting potential limit on the distances to SN Plio and SN Mio that is not dependent on the local interstellar low-density environment.

6.2. Local Bubble Implications

An interesting complexity arises when considering the solar system and the two near-Earth supernovae in conjunction with the large picture of the local Galactic neighborhood. The solar system is currently inside of the Local Bubble, a region defined by low densities and high temperatures which are the result of numerous supernova explosions in the last 20 Myr (Frisch 1981; Smith & Cox 2001; Frisch et al. 2011; Breitschwerdt et al. 2016; Zucker et al. 2022). Although not inside the Local Bubble at the time of its formation, Earth crossed into the region around 5 Mya (Zucker et al. 2022). The timing places SN Plio (3 Mya) within the Local Bubble and therefore its SNR's expansion and properties should be considered in the context of a very low-density ambient medium. However, the debris from SN Mio (7 Mya) arrived prior to the 5 Mya time of Earth's crossing into the Local Bubble, and thus its ^{60}Fe was delivered to us outside of the bubble. If SN Mio exploded outside the Local Bubble, it presumably expanded into a more general ISM medium; if SN Mio exploded inside the bubble, then the ^{60}Fe-bearing dust grains would have had to cross the Local Bubble wall in order to reach the solar system.

---

[16] The connection between the astrophysical loss of stratospheric ozone and biological damage is clearly complex and as yet little explored, but is beyond the scope of this paper. Future work on this topic would be of great use in clarifying the threat posed by nearby supernovae and similar astrophysical explosions.
[17] There are also no such events 7 Mya, for SN Mio.

---

[18] As a reminder, SN Mio was only measured in detail in 2021 (W21) and is therefore not considered in these evaluations, although we expect it to have similar results.

Examining these potential differences and their effects in detail is beyond the scope of this work, however this interconnected picture is something to keep in mind in further studies.

7. Conclusions

The distance to the 3 Mya supernova was last calculated using only two ^{60}Fe signal measurements (Fry et al. 2015). With the large range of new data (F16; L16; W16, W21), it is the perfect time to update this distance. We have also taken the opportunity to perform a parameter study on the astrophysical aspects of this problem and explore their effects on the supernova distance. The main points are listed below.

1. We have evaluated the distance to SN Plio using all available ^{60}Fe fluence data. This allows us to examine the consistency among these measurements. Comparison among the results hinges on the adopted uptake or incorporation efficiency, which varies among sites and groups; more study here would be useful. We find broad agreement among the measurements, some of which are independent.

2. Fixing $M_{\mathrm{ej},60} = 3 \times 10^{-5}\ M_\odot$ and $f_{60} = 10\%$, we find the distance to SN Plio (3 Mya) is $D \sim 20$–140 pc. The distance to SN Mio (7 Mya) for the same astronomical parameters is $D \sim 110$ pc—further variation is expected in this distance once more data have been analyzed.

3. While the range quoted above for SN Plio covers the full potential range of the data, more realistically the distance to SN Plio is between 50 and 65 pc. This accounts for the measurements by W16, W21, and F08, which fall inside the lunar range (F16), and this range is the approximate distance to Tuc–Hor, the stellar association most likely to host the CCSNe (Fry et al. 2015, 2020; Hyde & Pecaut 2018).

4. W21 measured both near-Earth supernova ^{60}Fe signals in the same FeMn crust sample; by using a ratio of the fluences from these measurements, we can portion the excess ^{60}Fe signal seen in the lunar regolith (F16) into the contributions from the two supernovae. We find that about 90% of the lunar signal is from SN Plio and about 10% is from SN Mio.

5. The sediment ^{60}Fe detections from L16 are a valuable contribution to the field; unfortunately, a distance calculation reveals that the fluence quoted in their work produces an unrealistically far distance. We must therefore suggest that their assumption of a 100% uptake factor was incorrect or that some of the ^{60}Fe in their samples was discarded.

6. The possible change in the uptake factor for the K04 data accounts for the entirety of the 20–140 pc range quoted for SN Plio—efforts to constrain this uptake factor will be of great value to the field and help narrow down the Earth-based spread in the distance range.

7. The astronomical parameters of ejected ^{60}Fe mass and dust fraction have a significant influence on the supernova distance and their possible values cover a wide range. We can say that combinations of low $M_{\mathrm{ej},60}$ and low f_{60} produce unrealistically close distances, while combinations of high $M_{\mathrm{ej},60}$ and high f_{60} lead to unrealistically far distances. For a supernova at about 50 pc, the combined parameter $f_{60} \times M_{\mathrm{ej},60} \simeq 2 \times 10^{-6}\ M_\odot$. Future observations that can shed new light on these parameters include CCSN dust measurements by JWST, and ^{60}Fe gamma-ray line measurements by the upcoming COSI mission (Tomsick & COSI Collaboration 2022).

8. The travel time parameter (how long the ^{60}Fe is traveling from production to deposition on Earth) has a negligible effect on the supernova distance.

The plethora of work that has gone into analyzing the ^{60}Fe signals over the last seven years has greatly increased our understanding of the two near-Earth supernovae; further efforts will help constrain the geophysical parameters in the distance calculations. We are especially interested in the results from sediment samples, as they are easiest to relate to the fluence of ^{60}Fe. Furthermore, sediment samples of the 7 Mya supernova will allow us to focus more closely on the astronomical differences between the two supernovae.

The field of supernova dust dynamics is an active area of research and applies to far more than what we have summarized in this paper. We look forward to advancements in the understanding of dust survival and destruction within remnants, as constraints on these numbers will help narrow our distance range. Investigations into ^{60}Fe production within supernovae and simulations of the explosion can also help tighten values for the ^{60}Fe ejected mass. Surveys, maps, and exploration of the Local Bubble allow further constraints on the distances to SN Plio and SN Mio. Observations of dust in supernovae, such as with JWST, can probe grain production and evolution. These independent measurements are invaluable, as they deal directly with the local neighborhood but are not correlated to the ^{60}Fe signals detected on Earth.

Finally, and regardless of any and all possible limiting effects, enough ^{60}Fe must travel from the supernovae to Earth to be detected by precision accelerator mass spectroscopy measurements *at least twice over* in the last 10 Myr. That such a signal has been observed twice in the (relatively) recent geologic past demonstrates that the process of getting the ^{60}Fe to Earth cannot overly inhibiting, and indeed suggests that the interstellar spread of supernova radioisotope ejecta may be a robust process.

ORCID iDs

Adrienne F. Ertel ● https://orcid.org/0000-0002-3876-2057
Brian D. Fields ● https://orcid.org/0000-0002-4188-7141

References

Altobelli, N., Kempf, S., Krüger, H., et al. 2005, JGRA, 110, A07102
Altobelli, N., Postberg, F., Fiege, K., et al. 2016, Sci, 352, 312
Athanassiadou, T., & Fields, B. D. 2011, NewA, 16, 229
Benítez, N., Maíz-Apellániz, J., & Canelles, M. 2002, PhRvL, 88, 81101/1
Bibron, R., Chesselet, R., Crozaz, G., et al. 1974, E&PSL, 21, 109
Binns, W. R., Israel, M. H., Christian, E. R., et al. 2016, Sci, 352, 677

Breitschwerdt, D., Feige, J., Schulreich, M. M., et al. 2016, Natur, 532, 73
Brunton, I. R., O'Mahoney, C., Fields, B. D., Melott, A. L., & Thomas, B. C. 2023, ApJ, 947, 42
Chaikin, E., Kaurov, A. A., Fields, B. D., & Correa, C. A. 2022, MNRAS, 512, 712
Cigan, P., Matsuura, M., Gomez, H. L., et al. 2019, ApJ, 886, 51
Costello, E. S., Ghent, R. R., & Lucey, P. G. 2018, Icar, 314, 327
Curtis, S., Ebinger, K., Fröhlich, C., et al. 2019, ApJ, 870, 2
Diehl, R., Lugaro, M., Heger, A., et al. 2021, PASA, 38, e062
Draine, B. T. T. 2011, The Physics of the Insterstellar and Intergalactic Medium (Princeton, NJ: Princeton Univ. Press)
Dwek, E., & Arendt, R. G. 2015, ApJ, 810, 75
Ejzak, L. M., Melott, A. L., Medvedev, M. V., & Thomas, B. C. 2007, ApJ, 654, 373
Ertel, A. F., Fry, B. J., Fields, B. D., & Ellis, J. 2023, ApJ, 947, 58
Fields, B. D., Athanassiadou, T., & Johnson, S. R. 2008, ApJ, 678, 549
Fields, B. D., & Ellis, J. 1999, NewA, 4, 419
Fields, B. D., Melott, A. L., Ellis, J., et al. 2020, PNAS, 117, 21008
Fields, B. D., & Wallner, A. 2023, ARNPS, 73, 365
Fimiani, L., Cook, D. L., Faestermann, T., et al. 2016, PhRvL, 116, 151104
Fitoussi, C., Raisbeck, G. M., Knie, K., et al. 2008, PhRvL, 101, 121101
Frisch, P. C. 1981, Natur, 293, 377
Frisch, P. C., Redfield, S., & Slavin, J. D. 2011, ARA&A, 49, 237
Fry, B. J., Fields, B. D., & Ellis, J. R. 2015, ApJ, 800, 71
Fry, B. J., Fields, B. D., & Ellis, J. R. 2016, ApJ, 827, 48
Fry, B. J., Fields, B. D., & Ellis, J. R. 2020, ApJ, 894, 109
Fuchs, B., Breitschwerdt, D., de Avillez, M. A., Dettbarn, C., & Flynn, C. 2006, MNRAS, 373, 993
Gehrels, N., Laird, C. M., Jackman, C. H., et al. 2003, ApJ, 585, 1169
Hyde, M., & Pecaut, M. J. 2018, AN, 339, 78
Kachelrieß, M., Neronov, A., & Semikoz, D. V. 2015, PhRvL, 115, 181103
Kachelrieß, M., Neronov, A., & Semikoz, D. V. 2018, PhRvD, 97, 063011
Knie, K., Korschinek, G., Faestermann, T., et al. 1999, PhRvL, 83, 18
Knie, K., Korschinek, G., Faestermann, T., et al. 2004, PhRvL, 93, 171103
Koll, D., Korschinek, G., Faestermann, T., et al. 2019, PhRvL, 123, 072701
Korschinek, G., Bergmaier, A., Faestermann, T., et al. 2010, NIMPB, 268, 187
Korschinek, G., & Faestermann, T. 2023, EPJA, 59, 52
Kutschera, W., Billquist, P. J., Frekers, D., et al. 1984, NIMPB, 5, 430
Limongi, M., & Chieffi, A. 2018, ApJS, 237, 13
Linde, T. J., & Gombosi, T. I. 2000, JGR, 105, 10411
Ludwig, P., Bishop, S., Egli, R., et al. 2016, PNAS, 113, 9232
Madronich, S., McKenzie, R., Björn, L., & Caldwell, M. 1998, JPPB, 46, 5
Mamajek, E. E. 2015, in IAU Symp. 314, Young Stars & Planets Near the Sun, ed. J. H. Kastner, B. Stelzer, & S. A. Metchev, 21
Mann, I. 2010, ARA&A, 48, 173

Marassi, S., Schneider, R., Limongi, M., et al. 2019, MNRAS, 484, 2587
Matsuura, M., De Buizer, J. M., Arendt, R. G., et al. 2019, MNRAS, 482, 1715
Matsuura, M., Dwek, E., Meixner, M., et al. 2011, Sci, 333, 1258
Matsuura, M., Indebetouw, R., Woosley, S., et al. 2017, MNRAS, 469, 3347
Melott, A. L., Marinho, F., & Paulucci, L. 2019, AsBio, 19, 825
Melott, A. L., & Thomas, B. C. 2011, AsBio, 11, 343
Melott, A. L., & Thomas, B. C. 2019, JG, 127, 475
Micelotta, E. R., Matsuura, M., & Sarangi, A. 2018, SSRv, 214, 53
Miller, J. A., & Fields, B. D. 2022, ApJ, 934, 32
Neuhäuser, R., Gießler, F., & Hambaryan, V. V. 2020, MNRAS, 498, 899
Nishiizumi, K., Imamura, M., Caffee, M. W., et al. 2007, NIMPB, 258, 403
Ostdiek, K. M., Anderson, T. S., Bauder, W. K., et al. 2017, PhRvC, 95, 055809
Rauscher, T., Heger, A., Hoffman, R. D., & Woosley, S. E. 2002, ApJ, 576, 323
Rozwadowska, K., Vissani, F., & Cappellaro, E. 2021, NewA, 83, 101498
Ruderman, M. A. 1974, Sci, 184, 1079
Rugel, G., Faestermann, T., Knie, K., et al. 2009, PhRvL, 103, 072502
Savchenko, V., Kachelrieß, M., & Semikoz, D. V. 2015, ApJL, 809, L23
Shahbandeh, M., Sarangi, A., Temim, T., et al. 2023, MNRAS, 523, 6048
Shindewolf, O. H. 1954, Neues Jahrb. Geol. Palaeontol. Monatshefte, 10, 457
Shklovskii, I. S., & Sagan, C. 1966, Intelligent Life in the Universe (San Francisco, CA: Holden-Day)
Silvia, D. W., Smith, B. D., & Michael Shull, J. 2010, ApJ, 715, 1575
Silvia, D. W., Smith, B. D., & Shull, J. M. 2012, ApJ, 748, 12
Slavin, J., Frisch, P., Heerikhuisen, J., et al. 2010, in COSPAR Scientific Assembly 38, 9
Slavin, J. D., Dwek, E., Mac Low, M.-M., & Hill, A. S. 2020, ApJ, 902, 135
Smith, R. K., & Cox, D. P. 2001, A&AS, 134, 283
Strub, P., Sterken, V. J., Soja, R., et al. 2019, A&A, 621, A54
Sukhbold, T., Ertl, T., Woosley, S. E., Brown, J. M., & Janka, H.-T. 2016, ApJ, 821, 38
Thomas, B. C. 2018, AsBio, 18, 481
Thomas, B. C., Engler, E. E., Kachelrieß, M., et al. 2016, ApJL, 826, L3
Thomas, B. C., & Yelland, A. M. 2023, ApJ, 950, 41
Tomsick, J. & COSI Collaboration 2022, ICRC (Berlin), 37, 652
Wallner, A. 2023, in Handbook of Nuclear Physics, ed. I. Tanihata, H. Toki, & T. Kajino (Singapore: Springer Nature), 1
Wallner, A., Bichler, M., Buczak, K., et al. 2015, PhRvL, 114, 041101
Wallner, A., Feige, J., Fifield, L. K., et al. 2020, PNAS, 117, 21873
Wallner, A., Feige, J., Kinoshita, N., et al. 2016, Natur, 532, 69
Wallner, A., Froehlich, M. B., Hotchkis, M. A. C., et al. 2021, Sci, 372, 742
Wanajo, S., Janka, H.-T., & Müller, B. 2013, ApJL, 774, L6
Wanajo, S., Müller, B., Janka, H.-T., & Heger, A. 2018, ApJ, 852, 40
Zucker, C., Goodman, A. A., Alves, J., et al. 2022, Natur, 601, 334